

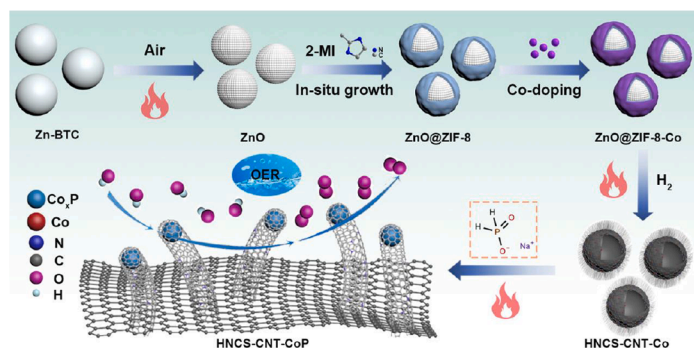
# Metal-organic framework derived hollow nitrogen-doped carbon sphere with cobalt phosphide in carbon nanotube for efficient oxygen evolution

Qihong Sun<sup>1</sup>, Jie Liu<sup>1</sup>, Xiangli Ji, Dandan Chen, Yuanyuan Guo, Lujiao Mao, Jinjie Qian<sup>\*</sup>

Key Laboratory of Carbon Materials of Zhejiang Province, College of Chemistry and Materials Engineering, Wenzhou University, Wenzhou, Zhejiang 325035, PR China

## GRAPHICAL ABSTRACT

Herein, we present the fabrication of a hollow TMP-based carbon material for efficient oxygen evolution reaction, employing a combined approach of MOF-assisted sacrificial template and epitaxial growth methods.



## ARTICLE INFO

### Keywords:

Metal-organic framework  
Hollow nanostructure  
Cobalt phosphide  
Carbon nanotube  
Oxygen evolution reaction

## ABSTRACT

The sluggish kinetics of the electrocatalytic oxygen evolution reaction (OER) pose a significant challenge in the field of overall water splitting. Transition metal phosphides have emerged as promising catalysts for OER by modulating the charge distribution of surrounding atoms. In this study, we employed self-sacrificing templates to fabricate hollow N-doped carbon spheres containing small-sized Co<sub>2</sub>P embedded within carbon nanotubes through high-temperature calcination and phosphorization, referred to as HNCS-CNT-CoP. The obtained HNCS-CNT-CoP electrocatalyst exhibited excellent OER performance in an alkaline electrolyte due to the optimization of OH\* adsorption energy and the large specific surface area created by the hollow structure. It demonstrated a low overpotential of 302 mV at a current density of 10 mA cm<sup>-2</sup> and a low Tafel slope of 68.5 mV dec<sup>-1</sup>, attributed to the electron transport facilitated by the *in situ* formed carbon nanotubes. Furthermore, theoretical calculations revealed a suitable reaction energy (1.17 eV) in the critical formation of Co<sub>2</sub>P\*OOH for HNCS-CNT-CoP, significantly lower than the rate-determining step of HNCS-CNT-Co (10.08 eV). These findings highlight the significance of hollow structures and Co<sub>2</sub>P-doping in the design of highly active non-noble metal OER electrocatalysts, enabling the reduction of energetic reaction barriers for future applications.

\* Corresponding author.

E-mail address: [jinjieqian@wzu.edu.cn](mailto:jinjieqian@wzu.edu.cn) (J. Qian).

<sup>1</sup> These authors contributed equally to this work.

<https://doi.org/10.1016/j.jcis.2023.09.082>

Received 19 June 2023; Received in revised form 8 September 2023; Accepted 11 September 2023

Available online 12 September 2023

0021-9797/© 2023 Elsevier Inc. All rights reserved.

## 1. Introduction

Electrocatalytic water splitting has emerged as a viable and sustainable approach to addressing energy demands and environmental concerns in the pursuit of a carbon-free economy [1–6]. However, the oxygen evolution reaction (OER) occurring at the anode presents a significant challenge due to its low efficiency and energy-intensive nature [7,8]. While noble-metal oxides like  $\text{RuO}_2$  and  $\text{IrO}_2$  have demonstrated effectiveness in enhancing the OER kinetics, their high cost and limited availability hinder widespread applicability [9,10]. Consequently, transition-metal phosphides (TMPs) with favorable d-orbital electron configurations have attracted attention as promising alternatives, owing to their cost-effectiveness and robust chemical stability [11–15]. Additionally, TMPs exhibit superior electrical conductivity in comparison to metal oxides or sulfides, which is advantageous for facilitating rapid charge transfer during electrocatalytic processes [16,17]. Nonetheless, the rational design and synthesis of multifunctional non-noble metal-based TMPs toward OER remain a formidable challenge [18].

Metal-organic frameworks (MOFs) have emerged as promising precursors for transition-metal phosphide (TMP) due to their large surface areas and tunable functional groups, garnering significant attention in the field of electrocatalytic water splitting [19–21]. Within this category, derivatives of zeolitic imidazolate framework (ZIF) possess inherently high graphitization and improved charge transport capabilities [22,23]. For instance, the integration of cobalt phosphide nanoparticles (NPs) into porous N-doped carbon derived from ZIF-67 showcases synergistic effects, where Co sites serve as hydroxyl acceptors and the negatively charged P atoms effectively capture protons, enhancing  $\text{O}_2$  desorption during OER [24–26]. However, traditional high-temperature pyrolysis methods often compromise ordered porous structures and lead to the aggregation of metal species [27]. In response, the formation of hollow nanostructures has been proposed as an effective strategy to curtail particle agglomeration and improve catalytic site exposure [28,29]. The presence of capacious voids within these hollow structures facilitates enhanced contact between exterior and interior surfaces, promoting efficient utilization of catalytic sites [30,31]. Therefore, the development of hollow-structured TMPs holds substantial promise for maximizing catalytic potential and augmenting long-term durability in water splitting.

Herein, we employed a comprehensive strategy that integrates MOF-assisted self-sacrificial templates and epitaxial growth methods to

fabricate one type of TMP-based carbon catalyst for efficient OER. This method enabled the formed  $\text{Co}_2\text{P}$  NPs within carbon nanotubes (CNTs) anchored onto hollow N-doped carbon spheres, denoted as HNCS-CNT-CoP, through the carbonization of imidazoles and simultaneous phosphorization of Co atoms (Scheme 1). The resulting hollow structure, along with the presence of multi-walled carbon CNTs, served to establish conductive pathways for efficient electron transfer and effectively mitigate the severe corrosion of  $\text{Co}_2\text{P}$  NPs. As an electrocatalyst for OER, HNCS-CNT-CoP demonstrated remarkable catalytic activity with a minimal overpotential of merely 302 mV at  $10 \text{ mA cm}^{-2}$  and satisfactory stability (91.8%) during a continuous 10-hour electrocatalytic operation. These superior performance stems from the unique hollow structure of HNCS-CNT-CoP, which not only provides abundant electrocatalytic active sites but also facilitates rapid charge and mass transportation.

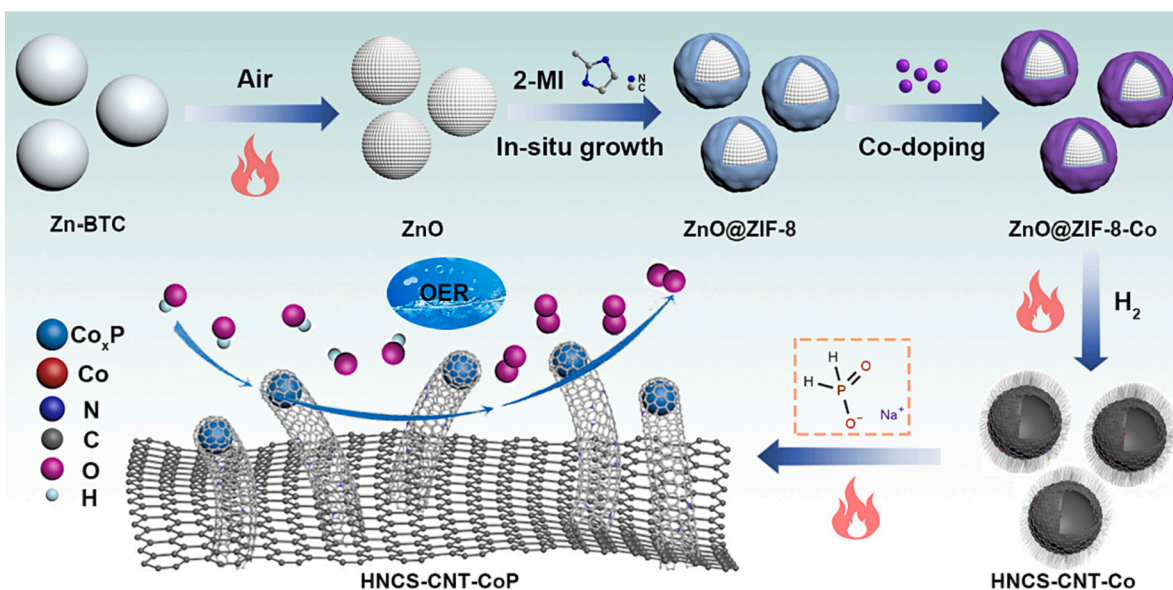
## 2. Experimental section

### 2.1. Chemicals

All chemicals were employed without further purification. Zinc nitrate hexahydrate ( $\text{Zn}(\text{NO}_3)_2 \cdot 6\text{H}_2\text{O}$ , AR, Aladdin), 2-methylimidazole (2-MI, AR, 99%, Aladdin), 1,3,5-benzenetricarboxylic acid ( $\text{H}_3\text{BTC}$ , 98%, Aladdin), dimethylacetamide (DMA, 99%, Aladdin), cobalt nitrate hexahydrate ( $\text{Co}(\text{NO}_3)_2 \cdot 6\text{H}_2\text{O}$ , AR, Aladdin), sodium hypophosphite ( $\text{NaH}_2\text{PO}_2 \cdot \text{H}_2\text{O}$ , 99%, Aladdin), distilled water and ethanol (EtOH, moisture content  $\leq 0.3\%$  from Aladdin, 99.9% from J&K) were used as received. JM 20 wt%  $\text{RuO}_2$  and 5 wt% Nafion ionomer were procured from Alfa-Aesar and Aldrich, respectively. All reagents were of analytical grade. All experiments were performed with high-purity  $\text{N}_2$ ,  $\text{O}_2$ ,  $\text{H}_2$ , Ar gases and distilled water.

### 2.2. Synthesis of Zn-BTC microspheres

Initially, 1,3,5-benzenetricarboxylic acid ( $\text{H}_3\text{BTC}$ , 90 mg) and zinc nitrate (186 mg) were dissolved in 60 mL of DMA in a pressure-resistant glass tube. The resulting solution was stirred for 20 min. Subsequently, the pressure-resistant glass tube was positioned in a heated aluminum block and maintained at  $150^\circ\text{C}$  for 30 min. Following this thermal treatment, the white product was separated from the mixture and subjected to multiple rounds of centrifugation. The obtained product was further washed three times with DMA and EtOH, and finally dried to



Scheme 1. Stepwise synthesis of hollow-structured and phosphatized HNCS-CNT-CoP for the efficient oxygen evolution.

obtain Zn-BTC microspheres [32]. Elemental analysis of Zn-BTC revealed: C, 35.25%; H, 3.14%; N, 2.56%.

### 2.3. Synthesis of ZnO microspheres

A quartz boat containing 200 mg of the prepared Zn-BTC was loaded into a chemical vapor deposition (CVD) tube furnace. The temperature was gradually raised at a rate of  $10\text{ }^{\circ}\text{C min}^{-1}$  until reaching  $500\text{ }^{\circ}\text{C}$ . The sample was held at this temperature for 30 min under an air atmosphere. Subsequently, the tube furnace was allowed to cool naturally to room temperature, resulting in the formation of ZnO microspheres. The yields of its derivative ZnO microspheres was approximately 30%.

### 2.4. Syntheses of ZnO@ZIF-8 and ZnO@ZIF-8-Co

First, 20 mg of as-prepared ZnO microspheres were dissolved in 4 mL of deionized water to create solution A. Solution B was prepared by dissolving 165 mg of 2-MI in 12 mL of DMA. Subsequently, solution B was rapidly added into solution A while maintaining agitation at 900 rpm and  $70\text{ }^{\circ}\text{C}$  for 5 h. Following the reaction period, the mixture was allowed to gradually cool to room temperature. The resulting white product was subjected to a thorough washing process using DMA and EtOH, followed by centrifugation. Finally, the obtained white product was dried at  $85\text{ }^{\circ}\text{C}$  for 12 h, yielding the core-shell ZnO@ZIF-8 material. To produce ZnO@ZIF-8-Co, the identical procedure was repeated for ZnO@ZIF-8 with the inclusion of 4 mg of  $\text{Co}(\text{NO}_3)_2$ . Subsequent to the reaction, the resultant mixture underwent washing, centrifugation, and drying, resulting in the formation of purple powder known as ZnO@ZIF-8-Co.

### 2.5. Syntheses of HNCS and HNCS-CNT-Co

To synthesize hollow N-doped carbon nanospheres (HNCS), a quartz boat containing ZnO@ZIF-8 (100 mg) was sealed and placed within a tube furnace. The furnace was initially purged with a mixed atmosphere of Ar (100 sccm) and  $\text{H}_2$  (100 sccm) for 5 min. The temperature was then ramped up to  $1000\text{ }^{\circ}\text{C}$  at a heating rate of  $20\text{ }^{\circ}\text{C min}^{-1}$  and maintained for 30 min. After cooling to room temperature, a black powder was obtained, representing the HNCS material. For the preparation of hollow N-doped carbon nanospheres rich in carbon nanotubes (HNCS-CNT-Co), the same procedure was employed as described above, with the substitution of ZnO@ZIF-8-Co in place of ZnO@ZIF-8. The yields of HNCS and HNCS-CNT-Co were calculated to be  $\sim 15\%$  after carbonization at  $1000\text{ }^{\circ}\text{C}$  from the composite precursors.

### 2.6. Synthesis of HNCS-CNT-CoP

In this experiment procedure, 20 mg of HNCS-CNT-Co was combined with  $\text{NaH}_2\text{PO}_2$  in a tube furnace, utilizing a mass ratio of 1:20. Subsequently, the resulting underwent pre-exhaustion within an Ar (100 sccm) atmosphere for 5 min. Following this pre-treatment step, the sample was subjected to carbonization, wherein the temperature was raised at a rate of  $10\text{ }^{\circ}\text{C min}^{-1}$ , attaining a final temperature of  $900\text{ }^{\circ}\text{C}$ , and then held steady at  $900\text{ }^{\circ}\text{C}$  for 2 h. After cooling naturally to room temperature, a black powder, denoted as HNCS-CNT-CoP, was obtained. The yields of HNCS-CNT-CoP was determined to be  $10\sim 15\%$  following carbonization at  $1000\text{ }^{\circ}\text{C}$  from the composite precursor materials [33].

### 2.7. Physical characterization

The obtained specimens were deposited onto meticulously cleaned silicon wafers for subsequent characterization. Field emission scanning electron microscopy (SEM) was employed to analyze their morphological features, while transmission electron microscopy (TEM) was utilized to observe lattice structures. Analysis of the crystalline surfaces and composition of the samples was conducted through Powder X-ray

diffraction (PXRD) patterns obtained from an X-ray diffractometer operating at 40 kV and 40 mA. Preceding  $\text{N}_2$  sorption assessments, thermal activation was carried out at  $100\text{ }^{\circ}\text{C}$  for 10 h.  $\text{N}_2$  isotherms were evaluated utilizing a Micromeritics ASAP 2020 analyzer. To investigate the carbon materials, Raman spectroscopy was carried out employing a laser micro Raman spectrometer with an excitation wavelength of 532 nm. Additionally, X-ray photoelectron spectroscopy (XPS) was conducted to analyze the elemental valence of the products.

### 2.8. Electrochemical analysis

(1) Preparation of three electrodes: All electrochemical measurements were conducted using a traditional three-electrode cell in a CHI760 electrochemical system. A platinum grid served as the counter electrode, while an  $\text{Hg}/\text{Hg}_2\text{Cl}_2$  electrode was used as the reference electrode, both immersed in a 1.0 M KOH solution. The reference electrode potential ( $E_{\text{RHE}}$ ) was corrected using the following equation:  $E_{\text{RHE}} = E_{\text{SCE}} + 0.2415\text{ V} + 0.059\text{ pH V}$ , where  $E_{\text{SCE}}$  is the measured potential relative to the saturated calomel electrode (SCE). The working electrodes were prepared as follows: the catalyst (2.5 mg) was dispersed in a mixture of ethanol (150  $\mu\text{L}$ ),  $\text{H}_2\text{O}$  (75  $\mu\text{L}$ ), and Nafion solution (5 wt%, 25  $\mu\text{L}$ ) using ultra-sonication. The resulting homogeneous suspension was dropwise added onto a polished glassy carbon electrode with a catalyst loading of  $\sim 0.2\text{ mg cm}^{-2}$ . The electrode was then dried at room temperature prior to electrochemical testing.

(2) Electrochemical test procedure: Linear sweep voltammetry (LSV) was performed with a scan rate of  $5\text{ mV s}^{-1}$  to study the electrochemical behavior. Electrochemical impedance spectroscopy (EIS) measurements were conducted over a frequency range of 1000 kHz to 0.01 Hz. The electrochemically active area (ECSA) was determined by conducting cyclic voltammetry (CV) tests at various sweep rates within the non-Faraday voltage window range. The electron transfer number was calculated using the ring-disk electrode (RRDE) technique. To minimize  $\text{O}_2$  interference on the disk electrode, the ring electrode potential was maintained at 0.40 V with a rotation speed of 1500 rpm. The Faraday efficiency (FE) was determined by analyzing the circle current, ring current, and the collection efficiency of the ring-disk electrode. Furthermore, the stability of the material was evaluated by subjecting it to a constant overpotential of 1.55 V vs. RHE for a duration of up to 10 h.

### 2.9. Theoretical calculation

The density functional theory was used to carry out all the calculations with the Perdew-Burke-Ernzerh exchange–correlation functional of generalized gradient approximation and the projector-augmented wave method, which was implemented through Vienna Ab-initio Simulation Package (VASP). The input model structure file is created by VESTA [34]. The plane wave-basis expansion cutoff energy was fixed at 450 eV, and atomic relaxation was conducted until the force exerted on atoms was less than  $0.02\text{ eV \AA}^{-1}$  and energy was concurrently converged to  $1 \times 10^{-6}\text{ eV}$ .

The Gibbs free energy change ( $\Delta G$ ) of each lithiation step was defined as:

$$\Delta G = \Delta E + \Delta ZPE - T\Delta S,$$

where  $\Delta E$  is the electronic energy difference directly obtained from DFT calculations,  $\Delta ZPE$  is the change in zero-point energy,  $T$  is the temperature ( $T = 298.15\text{ K}$ ) and  $\Delta S$  is the change in the entropy, respectively [35]. The zero-point energy and entropy were obtained through vibrational frequencies.

Conventionally, in an alkaline electrolyte, the anode reactions after oxygen adsorption can be written as:





### 3. Results and discussion

The facile synthesis process of core-shell ZnO@ZIF-8 and ZnO@ZIF-8-Co *via* seed epitaxial growth could be simply illustrated in Fig. 1a. First of all, SEM analysis revealed the smooth-surfaced Zn-BTC microspheres with an average size of 2.3  $\mu\text{m}$  (Fig. 1b, 1f, S1). A subsequent direct oxidation in air preserved the spherical morphology, yielding well-defined ZnO microspheres (Fig. 1c, 1g, S2-S3), characterized by a slightly rougher surface without significant shrinkage. Subsequent treatment involved the partial conversion of the ZnO surface into a ZIF-8 shell by introducing excessive 2-MI, resulting in complete coating with ZnO (Fig. 1d, 1h, S4). In this process, the added 2-MI ligand served both as an etchant to facilitate the dissolution of ZnO into Zn(II) ions and as a coordinated to form MOF shell [36]. Similarly, a ZIF-67 shell could also be developed atop the initial ZIF-8 shell, as indicated by the alteration in

powder color from white to purple (Fig. 1e, 1i, S5-S8). In Fig. 1j, the obtained ZnO exhibited diffraction peaks that perfectly matched with ZnO (JCPDS-PDF#65-3411) [32], where the peaks located at 31.5°, 34.3° and 36.3° were assigned to the (100), (002), and (101) planes, respectively. Conversely, the diffraction angles at 7.4°, 10.7°, and 12.7° observed in ZnO@ZIF-8 and ZnO@ZIF-8-Co aligned with the simulated MOF patterns. Notably, the N<sub>2</sub> isotherms of both Zn-BTC and ZnO exhibited characteristic Type-III curves, while the desolvated samples with MOF shells displayed Type-I isotherms, consistent with the trend observed in pore size distribution (PSD) (Fig. 1k). Lastly, the total pore volumes of MOF-containing samples were significantly higher at 0.16 and 0.35  $\text{cm}^3 \text{g}^{-1}$ , respectively, while the specific surface area of ZnO@ZIF-8-Co (425.2  $\text{m}^2 \text{g}^{-1}$ ) surpassed that of ZnO@ZIF-8 (238.8  $\text{m}^2 \text{g}^{-1}$ ) as documented in Table S1. The carbonization process of ZnO-based precursors led to the evaporation of most internal Zn species, culminating in the formation of hollow nanostructures. SEM and TEM images (Fig. 2a-2f, S9-S10) revealed the preservation of intact hollow morphology across all carbon materials. Among them, HNCS-CNT-Co was distinguished by the presence of numerous multi-walled CNTs onto the carbon surface, attributed to the efficacious catalytic action of

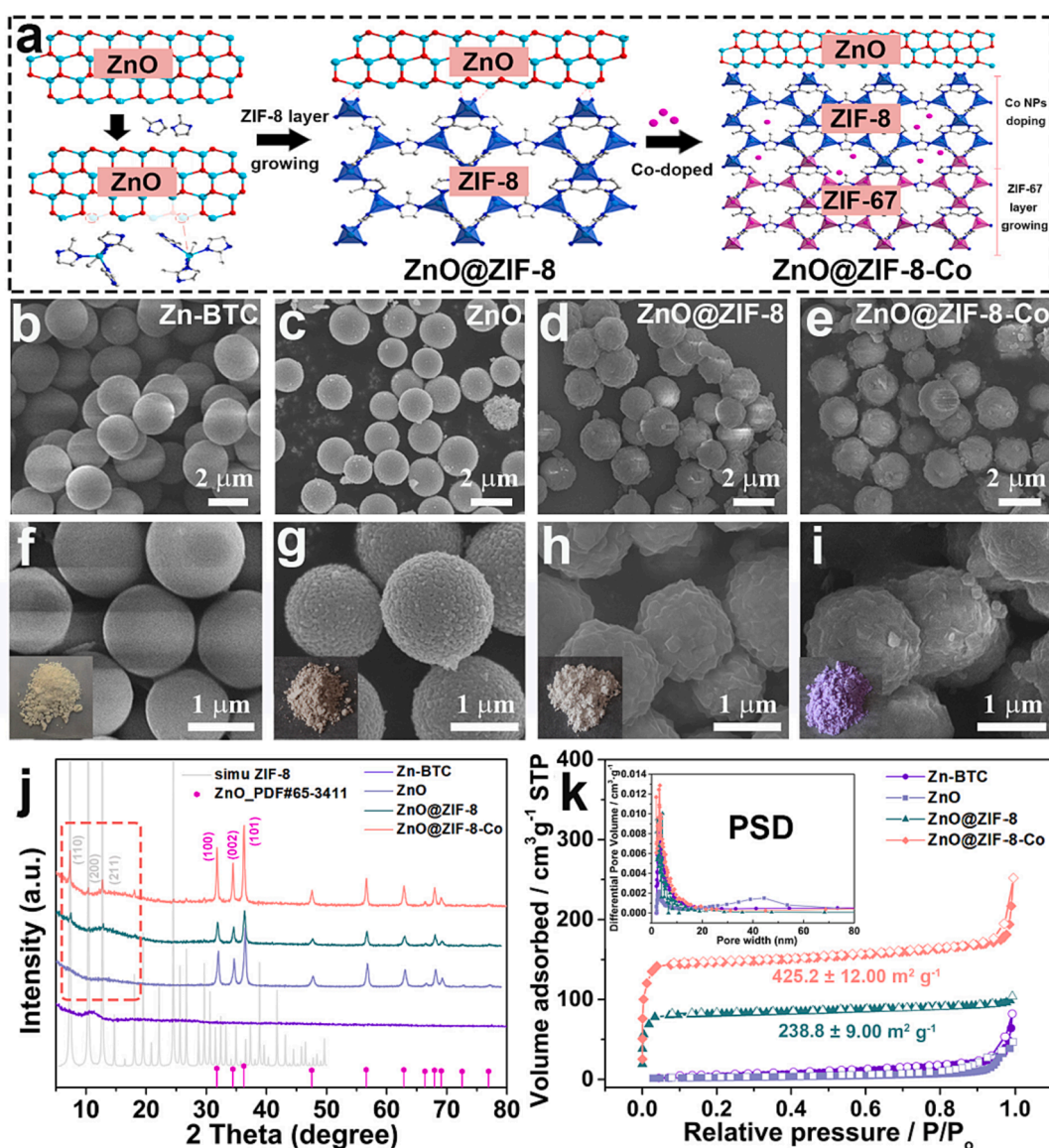


**Fig. 1.** (a) Stepwise synthesis of ZnO@ZIF-8-Co. SEM images of (b/f) Zn-BTC, (c/g) ZnO, (d/h) ZnO@ZIF-8 and (e/i) ZnO@ZIF-8-Co; (j) PXRD patterns; (k) N<sub>2</sub> isotherms and PSD curves (inset).

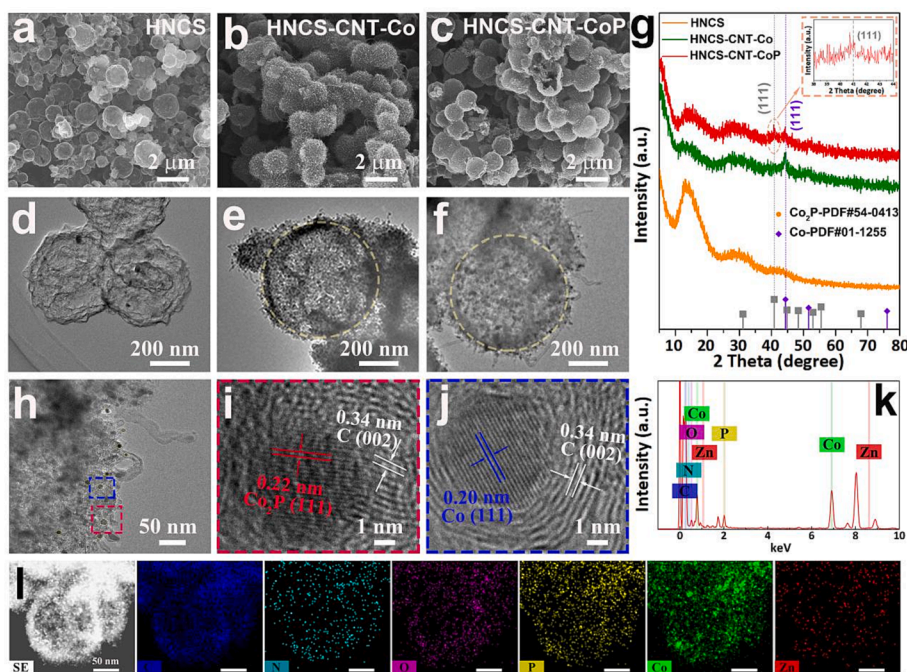


**Fig. 2.** SEM/TEM images of (a/d) HNCS, (b/e) HNCS-CNT-Co and (c/f) HNCS-CNT-CoP; (g) PXRD patterns, (h-j) HRTEM images, (k) EDS spectrum and (l) elemental mappings of HNCS-CNT-CoP.

Co NPs (Fig. 2b, 2e, S11-S12) [37]. HNCS-CNT-Co further underwent a phosphatization process, resulting in P-atom doping while maintaining the integrity of the hollow structure and the presence of surface-grown CNTs (Fig. 2c, 2f, S13-S15). Fig. 2g showed that HNCS-CNT-Co exhibited a characteristic diffraction peak at  $44.2^\circ$ , corresponding to the (1 1 1) crystal plane of metallic Co (JCPDS-PDF#01-1255) [38]. In contrast, HNCS-CNT-CoP displayed the Co diffraction peak and an additional peak at  $40.8^\circ$  assigned to the (1 1 1) crystal plane of  $\text{Co}_2\text{P}$  (JCPDS-PDF#54-0413) [39]. Furthermore, Fig. 2h-2j revealed lattice fringes measuring 0.22 and 0.20 nm within HNCS-CNT-CoP, corresponding to the (1 1 1) plane of  $\text{Co}_2\text{P}$  and the (1 1 1) plane of Co, respectively. The spacing of 0.34 nm between adjacent carbon layers was ascribed to the graphite carbon (0 0 2) surface. Energy dispersive spectroscopy (EDS) and element mapping images demonstrated a uniform dispersion of Co, P, and N elements throughout the carbon matrix (Fig. 2k, 2l). The non-agglomeration of Co NPs could be attributed to the presence of ZIF-8 within the precursor. This spatial isolation allows for the relatively dispersed and homogeneous distribution of Co/ $\text{Co}_2\text{P}$  NPs in Fig. S16, thereby facilitating subsequent electrocatalytic reactions.

Raman spectra were collected to characterize and compare the degree of graphitization in the investigated carbon nanomaterials (Fig. 3a). Notably, two distinct Raman peaks were identified at 1331 and

$1577\text{ cm}^{-1}$ , corresponding to defective or disordered carbon and graphitic carbon, respectively [40]. The relative intensity ratios of the D band to the G band ( $I_D/I_G$ ) were calculated for HNCS-CNT-CoP (1.23) and HNCS-CNT-Co (1.08). These values were much lower than that of HNCS (1.58), indicating that the presence of multi-walled CNTs contributes to enhanced graphitization degree. Phosphorization resulted in the formation of cobalt phosphide, inducing partial degradation of the graphitic carbon layer and consequently increasing defects in HNCS-CNT-CoP. The hysteresis loops observed in Fig. 3b-3c indicated Type-IV isotherms for all three catalysts, confirming the existence of mesoporous structures. The specific surface areas of HNCS, HNCS-CNT-Co, and HNCS-CNT-CoP were determined as 142.8, 161.3, and  $112.0\text{ m}^2\text{ g}^{-1}$ , respectively, along with pore volumes listed in Table S1. In this case, the growth of cobalt phosphide led to a partial obstruction of certain pores, resulting in slightly elevated specific surface area and pore volume in unphosphatized HNCS-CNT-Co. Overall, the formed CNTs effectively enhance the pore environment and conductivity, thereby facilitating efficient electron transfer among the active materials.

The X-ray photoelectron spectroscopy (XPS) analysis presented in Fig. 4a and S17-S19 confirmed the presence of C, N, O, Co, P, and Zn elements for HNCS-CNT-CoP. In the high-resolution C 1 s spectrum (Fig. 4b), four main peaks were discerned: C–C (284.8 eV), C–N

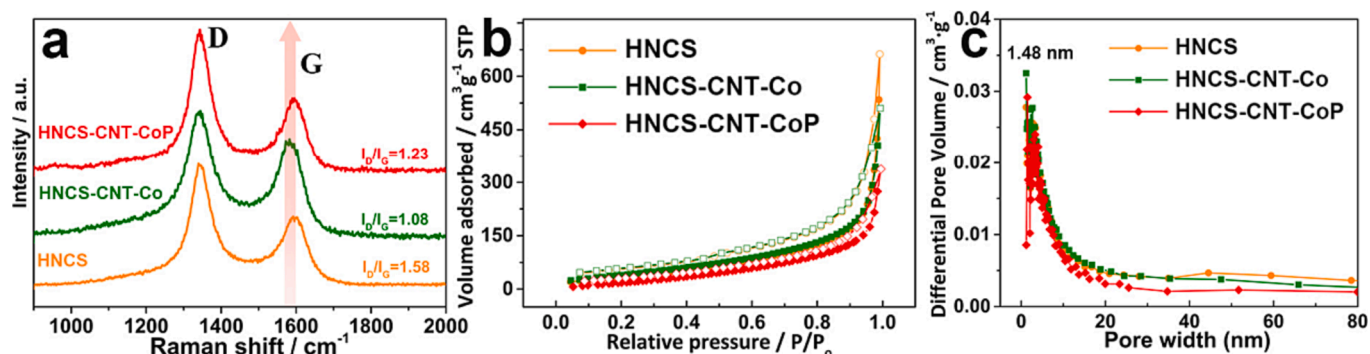


**Fig. 3.** (a) Raman spectra, (b)  $\text{N}_2$  isotherms and (c) PSD curves of HNCS, HNCS-CNT-Co and HNCS-CNT-CoP.

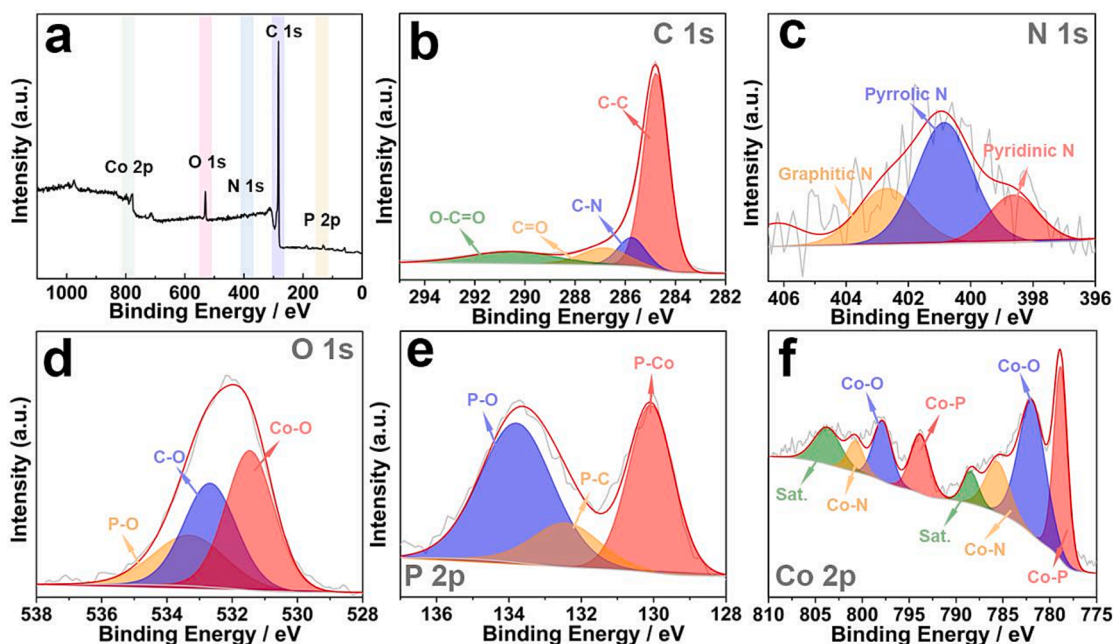


Fig. 4. (a) XPS full spectrum of HNCS-CNT-CoP; The deconvoluted spectra of (b) C 1s, (c) N 1s, (d) O 1s, (e) P 2p and (f) Co 2p for HNCS-CNT-CoP.

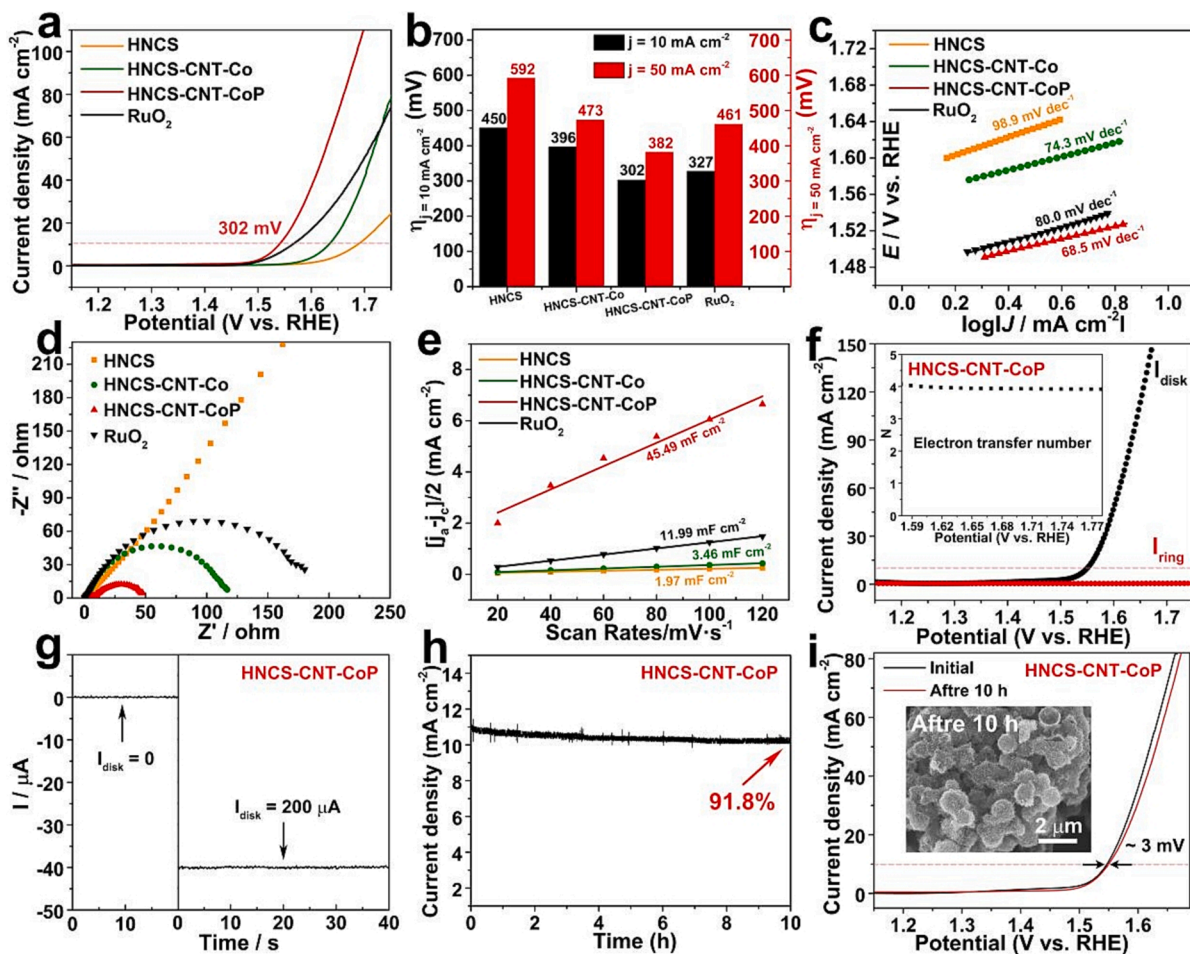


Fig. 5. (a) LSV curves; (b) The overpotential comparison; (c) Tafel plots; (d) Nyquist curves; (e)  $C_{dl}$  plots; (f/g) LSV curves/ring current of HNCS-CNT-CoP on RRDE; (h) Chronoamperometry at 1.52 V and (i) LSV curves of HNCS-CNT-CoP before and after 10 h.

(285.7 eV), C=O (286.9 eV), and O=C=O (290.5 eV), indicating a significant content of hybrid carbon and abundant defect sites. The deconvoluted N 1s spectrum (Fig. 4c) showed three peaks at 398.6, 400.8, and 402.7 eV, corresponding to pyridinic N, pyrrolic N, and graphitic N, respectively. The presence of graphitic N and pyridinic N is anticipated to augment the overall electrocatalytic performance by acting as active adsorption species [41]. Within the O 2p spectrum revealed three oxygen species at 531.5, 532.7, and 533.4 eV, attributed to Co-O, C-O, and P-O, respectively (Fig. 4d). Moreover, the deconvoluted P 2p spectrum in Fig. 4e displayed three main peaks at 130.1, 132.5, and 133.8 eV, corresponding to P-Co, P-C, and P-O, respectively. In the Co 2p region, discernible peaks assigned to Co-P were observed at 778.9 and 793.8 eV, indicative of higher binding energy compared to HNCS-CNT-Co (Fig. 4f, S20). This suggests electron transfer from Co to P owing to the elevated electronegativity of P atoms, leading to lattice distortion and modification of electronic structure at the atomic level, thereby amplifying the intrinsic activity of HNCS-CNT-CoP [42]. Peaks situated at 782.1 and 797.9 eV, along with two satellite peaks approximately at 788.5 and 803.9 eV, were attributed to oxidized species resulting from the partial oxidation of phosphide. Additional peaks in the Co 2p spectrum could be attributed to the Co-N bond (785.6 and 800.8 eV), signifying robust electronic coupling between Co species and N-doped carbon, facilitating charge transfer at the catalytic active site.

The OER activity of carbon-based electrocatalysts was initially

assessed using linear sweep voltammetry (LSV) in Fig. 5a. Remarkably, HNCS-CNT-CoP exhibited notably lower overpotential ( $\eta_{10/50}$ ) values of 302/382 mV at 10/50 mA cm<sup>-2</sup> (Fig. 5b) compared to RuO<sub>2</sub> (327/461 mV), HNCS (450/592 mV), and HNCS-CNT-Co (396/473 mV). The Tafel slopes for HNCS-CNT-CoP, RuO<sub>2</sub>, HNCS, and HNCS-CNT-Co were determined to be 68.5, 80.0, 98.9, and 74.3 mV dec<sup>-1</sup>, respectively, indicating the superior catalytic kinetics for HNCS-CNT-CoP (Fig. 5c). In Fig. 5d, electrochemical impedance spectroscopy (EIS) confirmed that the order of charge transfer resistance as HNCS-CNT-CoP < HNCS-CNT-Co < RuO<sub>2</sub> < HNCS, aligning well with the LSV and Tafel results. To further underscore the effectiveness of phosphorization, the electrochemically active surface area (ECSA) was further calculated by measuring the double layer capacitance ( $C_{dl}$ ). Evidently, HNCS-CNT-CoP showed a much higher  $C_{dl}$  value (45.49 mF cm<sup>-2</sup>) compared with RuO<sub>2</sub> (11.99 mF cm<sup>-2</sup>), HNCS (1.97 mF cm<sup>-2</sup>), and HNCS-CNT-Co (3.46 mF cm<sup>-2</sup>), indicating an increased number of defect sites induced during the phosphorization process (Fig. 5e, S21). Furthermore, Fig. 5f, S22 demonstrated that the negligible ring current ( $I_{ring}$ ) in relation to the disk current ( $I_{disk}$ ), indicating that the OER reaction on the HNCS-CNT-CoP catalyst closely followed a 4-electron transfer process. The Faradaic efficiency (FE) was verified using the RRDE technique to present a detected  $I_{ring}$  of ~39.6  $\mu$ A and a remarkably high FE of 100% at a fixed  $I_{disk}$  of 200  $\mu$ A (Fig. 5g, S23). The endurance of HNCS-CNT-CoP in OER was assessed using a chronopotential curve in Fig. 5h, S24, demonstrating an impressive current density retention of nearly 91.8% at a

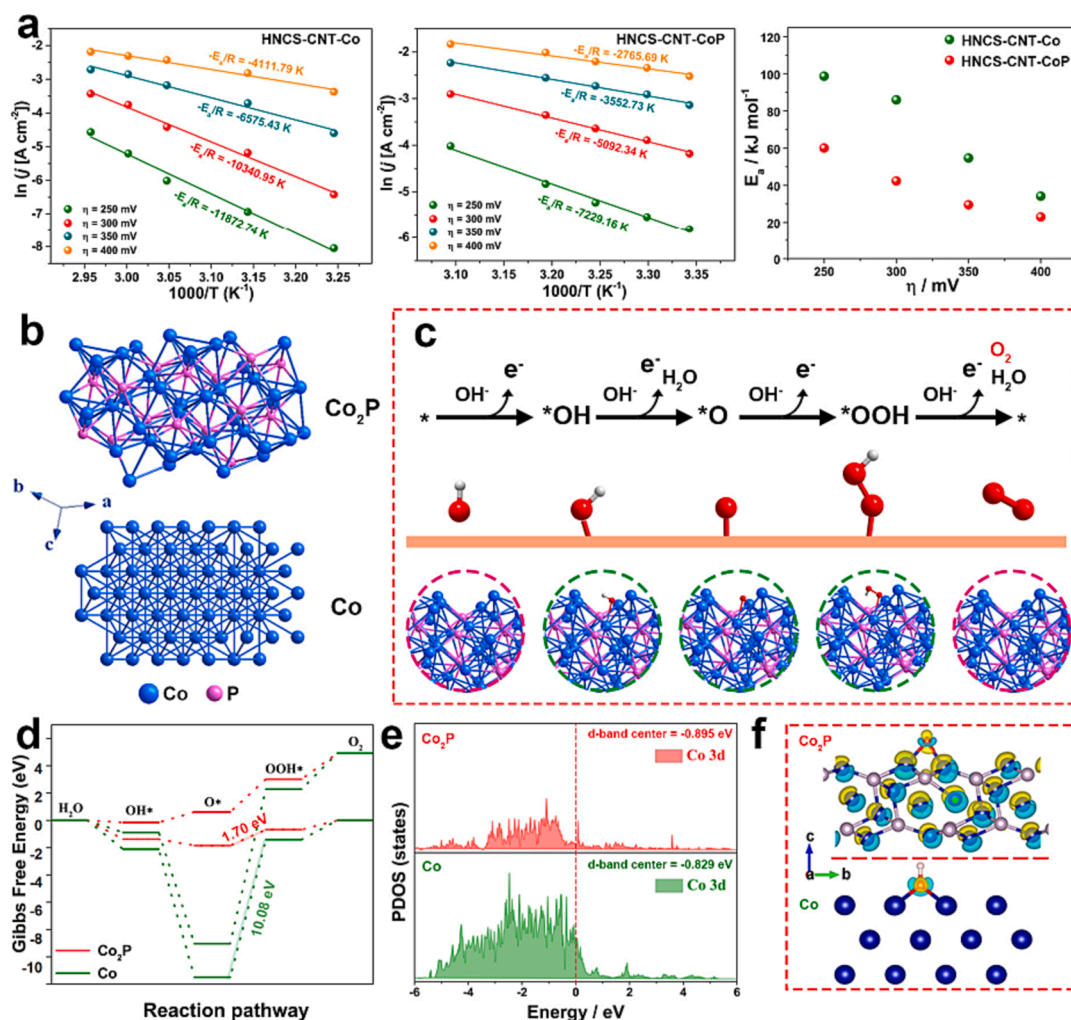


Fig. 6. (a) Arrhenius plots and  $E_a$  of Co<sub>2</sub>P and Co; (b) Optimized atomic structures of Co<sub>2</sub>P and Co; (c) Schematic illustration of the OER mechanism for Co<sub>2</sub>P; (d) Gibbs free-energy diagram, (e) The calculated PDOS curves and (f) The charge density difference plots for Co<sub>2</sub>P-\*OH and Co-\*OH.

constant potential of 1.52 V over a 10-hour duration. Minimal variation of approximately 3 mV was observed in the LSV curves before and after the Chronoamperometric test (Fig. 5i). Additionally, extended testing at a constant potential of 1.52 V for 500 h was conducted as shown in Fig. S24, underscoring the catalyst's capability to uphold a current density of up to 80.54%. SEM and TEM characterization following the electrochemical test further confirmed the well-preserved hollow morphology of the catalyst, thereby substantiating its robust long-term stability (Fig. S25–26). These findings emphasize the advantageous synergy derived from P-doping and the hollow structure of HNCS-CNT-CoP, contributing to heightened conductivity, promoting electron transfer, and the provision of abundant active sites for efficient OER. This positions HNCS-CNT-CoP as a competitive candidate among the previously reported Co-based electrocatalysts listed in Table S2.

We systematically assessed the OER performance of two catalysts, namely HNCS-CNT-CoP and HNCS-CNT-Co, at different temperatures and subsequently analyzed the activation energy ( $E_a$ ) of these samples. Fig. S27 depicts the increasing trend of OER current for both catalysts as electrolyte temperature rises. Upon examination of the Arrhenius plots in Fig. 6a, it becomes evident that the calculated  $E_a$  values for HNCS-CNT-CoP, at varying overpotentials, are notably lower than those observed for HNCS-CNT-Co. This suggests that the further phosphidation of the material induces alterations in its electronic structure, thereby enhancing catalytic activity. Furthermore, we conducted density functional theory (DFT) calculations, focusing on the constructed  $\text{Co}_2\text{P}$  and Co structures based on the (111) surface, to gain deeper insights into their respective OER behavior (Fig. 6b). The theoretical analysis involves four consecutive proton-coupled electron transfer steps, giving rise to the generation of three intermediate species ( $^*\text{OH}$ ,  $^*\text{O}$ , and  $^*\text{OOH}$ ) as shown in Fig. 6c, S28–29, [15] Fig. 6d, Table S3 illustrate that all the OER steps associated with  $\text{Co}_2\text{P}$  involve energetically uphill processes at  $U = 1.23$  V. The third step, which involves the formation of  $\text{Co}_2\text{P}^*\text{OOH}$ , acts as the rate-determining step (RDS) for  $\text{Co}_2\text{P}$ , exhibiting an energy barrier of 1.17 eV, significantly lower than the RDS of Co (10.08 eV). The partial density of states (PDOS, Fig. 6e) reveals that the center energy of the d-band of  $\text{Co}_2\text{P}$  (−0.895 eV) is comparatively lower than that of Co (−0.829 eV). Further insight into the electronic structure is offered through the charge density difference plots of  $\text{Co}_2\text{P}$  and Co (Fig. 6f, S30). These plots visually demonstrate the formation of covalent bonds between P atoms and Co atoms, resulting in an intensified electron cloud density around the Co sites within the coordinated environment. This intricate electronic interaction fosters an environment conducive to enhancing both the rate and efficiency of the OER reaction.

#### 4. Conclusion

In this study, we have successfully fabricated multi-level porous carbon nanomaterials by utilizing a self-sacrificing template involving amorphous Zn-BTC microsphere. Controlled phosphorization coupled with carbonization treatment led to the formation of hollow N-doped carbon spheres housing  $\text{Co}_2\text{P}$  NPs within a matrix of multi-walled CNTs. The optimized HNCS-CNT-CoP exhibited a markedly improved OER activity with lower overpotential of a mere 302 mV at  $10 \text{ mA cm}^{-2}$  and Tafel slope of  $68.5 \text{ mV dec}^{-1}$  than other similar materials in the literatures [43,44]. Moreover, it also showcased commendable long-term stability, positioning HNCS-CNT-CoP as a promising non-noble metal electrocatalyst. Furthermore, corroborative theoretical calculations confirmed the critical step involving the formation of  $\text{Co}_2\text{P}^*\text{OOH}$  as the RDS for HNCS-CNT-CoP, marked by a remarkably low energy barrier of 1.17 eV, a distinct advantage when compared to its control counterpart. The surface modification strategy advanced in this work represents a novel approach toward the development of high-performance catalysts for practical applications in overall water splitting.

#### CRedit authorship contribution statement

**Qihong Sun:** Methodology, Data curation, Formal analysis, Investigation, Validation, Writing – original draft. **Jie Liu:** Methodology, Data curation, Formal analysis. **Xiangli Ji:** Data curation, Formal analysis, Writing – original draft. **Dandan Chen:** Data curation, Formal analysis. **Yuanyuan Guo:** Data curation, Formal analysis. **Lujiao Mao:** Data curation, Formal analysis. **Jinjie Qian:** Conceptualization, Formal analysis, Funding acquisition, Investigation, Project administration, Supervision.

#### Declaration of Competing Interest

The authors declare that they have no known competing financial interests or personal relationships that could have appeared to influence the work reported in this paper.

#### Data availability

Data will be made available on request.

#### Acknowledgments

This work was financially supported by National Natural Science Foundation of China (21601137), Natural Science Foundation of Zhejiang Province (LQ16B010003), Basic Science and Technology Research Project of Wenzhou, Zhejiang Province (H20220001), and the Special Basic Cooperative Research Programs of Yunnan Provincial Undergraduate Universities Association (202101BA070001-042).

#### Appendix A. Supplementary data

Supplementary data to this article can be found online at <https://doi.org/10.1016/j.jcis.2023.09.082>.

#### References

- [1] N. Suen, S. Hung, Q. Quan, et al., Electrocatalysis for the oxygen evolution reaction: recent development and future perspectives, *Chem. Soc. Rev.* 46 (2017) 337–365.
- [2] Y. Zeng, M. Zhao, Z. Huang, et al., Surface reconstruction of water splitting electrocatalysts, *Adv. Energy Mater.* 12 (2022) 2201713.
- [3] L. Huang, R. Yao, X. Wang, et al., In situ phosphating of Zn-doped bimetallic skeletons as a versatile electrocatalyst for water splitting, *Energ. Environ. Sci.* 15 (2022) 2425–2434.
- [4] J. Turner, Sustainable hydrogen production (review), *Science*, 305: 972–974.
- [5] M. Wang, X. Chen, H. Yao, et al., Research progress in lithium-excess disordered rock-salt oxides cathode, *Energy Environ. Mater.* 5 (2022) 1139–1154.
- [6] Y. Guo, S. Wu, Y. He, et al., Solid-state lithium batteries: Safety and prospects, *eScience* 2 (2022) 138–163.
- [7] K. Wang, X. Wang, Z. Li, et al., Designing 3d dual transition metal electrocatalysts for oxygen evolution reaction in alkaline electrolyte: beyond oxides, *Nano Energy* 77 (2020), 105162.
- [8] Q. Lu, Y. Guo, P. Mao, et al., Rich atomic interfaces between sub-1 nm  $\text{RuO}_x$  clusters and porous  $\text{Co}_3\text{O}_4$  nanosheets boost oxygen electrocatalysis bifunctionality for advanced Zn-air batteries, *Energy Storage Mater.* 32 (2020) 20–29.
- [9] F. Frame, T. Townsend, R. Chamousis, et al., Photocatalytic water oxidation with nonsensitized  $\text{IrO}_2$  nanocrystals under visible and UV light, *J. Am. Chem. Soc.* 133 (2011) 7264–7267.
- [10] Q. Yang, G. Li, K. Manna, et al., Topological engineering of Pt-group-metal-based chiral crystals toward high-efficiency hydrogen evolution catalysts, *Adv. Mater.* 32 (2020) 1908518.
- [11] H. Liao, Y. Sun, C. Dai, et al., An electron deficiency strategy for enhancing hydrogen evolution on CoP nano-electrocatalysts, *Nano Energy* 50 (2018) 273–280.
- [12] D. Yang, Y. Chen, Z. Su, et al., Organic carboxylate-based MOFs and derivatives for electrocatalytic water oxidation, *Coord. Chem. Rev.* 428 (2021), 213619.
- [13] B. Liu, R. Wang, Y. Yao, et al., Hollow-structured CoP nanotubes wrapped by N-doped carbon layer with interfacial charges polarization for efficiently boosting oxygen reduction/evolution reactions, *Chem. Eng. J.* 431 (2022), 133238.
- [14] V. Ganesan, J. Kim, S. Radhakrishnan, CoP embedded in hierarchical N-doped carbon nanotube frameworks as efficient catalysts for the hydrogen evolution reaction, *ChemElectroChem* 5 (2018) 1644–1651.

- [15] D. Park, M.-H. Kim, M. Kim, et al., Spherical nickel doped cobalt phosphide as an anode catalyst for oxygen evolution reaction in alkaline media: From catalysis to system, *Appl. Catal. B Environ.* 327 (2023), 122444.
- [16] Y. Shi, B. Zhang, Recent advances in transition metal phosphide nanomaterials: synthesis and applications in hydrogen evolution reaction, *Chem. Soc. Rev.* 45 (2016) 1529–1541.
- [17] K. Fan, H. Chen, Y. Ji, et al., Nickel-vanadium monolayer double hydroxide for efficient electrochemical water oxidation, *Nat. Commun.* 7 (2016) 11981.
- [18] Z. Lu, Y. Gao, J. Xie, et al., Construction of Co<sub>2</sub>P/CoP@Co@NCNT rich-interface to synergistically promote overall water splitting, *Chem. Eng. J.* 430 (2022), 132877.
- [19] L.i. Song, Y. Gao, N. Li, et al., Transition metal-based bimetallic MOFs and MOF-derived catalysts for electrochemical oxygen evolution reaction, *Energ. Environ. Sci.* 14 (2021) 1897–1927.
- [20] S. Li, T. Wang, D. Tang, et al., Metal-organic framework integrating ionic framework and bimetallic coupling effect for highly efficient oxygen evolution reaction, *Adv. Sci.* 2203712 (2022).
- [21] J. Tian, F. Jiang, D. Yuan, et al., Electric-field assisted in situ hydrolysis of bulk metal-organic frameworks (MOFs) into ultrathin metal oxyhydroxide nanosheets for efficient oxygen evolution, *Angew. Chem. Int. Ed.* 59 (2020) 13101–13108.
- [22] H. Jadhav, H. Bandal, S. Ramakrishna, et al., Critical review, recent updates on zeolitic imidazolate framework-67 (ZIF-67) and its derivatives for electrochemical water splitting, *Chem. Eng. J.* 403 (2021), 126371.
- [23] X. Gu, Z. Liu, H. Liu, et al., Fluorination of ZIF-67 framework templated Prussian blue analogue nano-box for efficient electrochemical oxygen evolution reaction, *Chem. Eng. J.* 403 (2021), 126371.
- [24] M. Liu, J. Li, Cobalt phosphide hollow polyhedron as efficient bifunctional electrocatalysts for the evolution reaction of hydrogen and oxygen, *ACS Appl. Mater. Inter.* 8 (2016) 2158–2165.
- [25] Y. Pan, K. Sun, S. Liu, et al., Core-shell ZIF-8@ZIF-67-derived CoP nanoparticle-embedded N-doped carbon nanotube hollow polyhedron for efficient overall water splitting, *J. Am. Chem. Soc.* 140 (2018) 2610–2618.
- [26] J. Yu, Y. Zhong, X. Wu, et al., Bifunctionality from synergy: CoP nanoparticles embedded in amorphous CoO<sub>x</sub> nanoplates with heterostructures for highly efficient water electrolysis, *Adv. Sci.* 5 (2018) 1800514.
- [27] J. Wang, F. Ciucci, In-situ synthesis of bimetallic phosphide with carbon tubes as an active electrocatalyst for oxygen evolution reaction, *Appl. Catal. B Environ.* 254 (2019) 292–299.
- [28] Z. Li, M. Song, W. Zhu, et al., MOF-derived hollow heterostructures for advanced electrocatalysis, *Coord. Chem. Rev.* 439 (2021), 213946.
- [29] M. Yang, C. Zhang, N. Li, et al., Design and synthesis of hollow nanostructures for electrochemical water splitting, *Adv. Sci.* 9 (2022) 2105135.
- [30] B. Li, H. Zeng, Architecture and preparation of hollow catalytic devices, *Adv. Mater.* 31 (2019) 1801104.
- [31] Y. Wang, M. Yang, Y. Ding, et al., Recent advances in complex hollow electrocatalysts for water splitting, *Adv. Funct. Mater.* 32 (2022) 2108681.
- [32] L. Chai, L. Zhang, X. Wang, et al., Bottom-up synthesis of MOF-derived hollow N-doped carbon materials for enhanced ORR performance, *Carbon* 146 (2019) 248–256.
- [33] Y. Guo, Q. Sun, Q. Huang, et al., Variable HOF-derived carbon-coated cobalt phosphide for electrocatalytic oxygen evolution, *Carbon* 196 (2022) 457–465.
- [34] K. Momma, F. Izumi, VESTA 3 for three-dimensional visualization of crystal, volumetric and morphology data, *J. Appl. Cryst.* 44 (2011) 1272–1276.
- [35] J. Cao, X. Zhang, S. Zhao, et al., Mechanism of the two-dimensional WSeTe/Zr<sub>2</sub>CO<sub>2</sub> direct Z-scheme van der Waals heterojunction as a photocatalyst for water splitting, *PCCP* 24 (2022) 21030–21039.
- [36] Q. Sun, D. Chen, Q. Huang, et al., Carbon nanotubes anchored onto hollow carbon for efficient oxygen reduction, *Sci. China Mater.* 66 (2023) 641–650.
- [37] R. Wang, R. Wu, X. Yan, et al., Implanting single Zn atoms coupled with metallic Co nanoparticles into porous carbon nanosheets grafted with carbon nanotubes for high-performance lithium-sulfur batteries, *Adv. Funct. Mater.* 32 (2022) 2200424.
- [38] H. Noh, K. Lee, P. Chandra, et al., Application of a Cu-Co alloy dendrite on glucose and hydrogen peroxide sensors, *Electrochim. Acta* 61 (2012) 36–43.
- [39] D. Zhou, L. Fan, Co<sub>2</sub>P nanoparticles encapsulated in 3D porous N-doped carbon nanosheet networks as an anode for high-performance sodium-ion batteries, *J. Mater. Chem. A* 6 (6) (2018) 2139–2147.
- [40] D. Zhang, J. Yang, M. Li, et al., (*n, m*) Assignments of metallic single-walled carbon nanotubes by Raman spectroscopy: The importance of electronic raman scattering, *ACS Nano* 10 (2016) 10789–10797.
- [41] Y. Xiong, H. Li, C. Liu, et al., Single-atom Fe catalysts for Fenton-like reactions: Roles of different N species, *Adv. Mater.* 34 (2022) 2110653.
- [42] X. Wang, H. Huang, J. Qian, et al., Intensified Kirkendall effect assisted construction of double-shell hollow Cu-doped CoP nanoparticles anchored by carbon arrays for water splitting, *Appl. Catal. B Environ.* 325 (2023), 122295.
- [43] Y. Guo, Q. Huang, J. Ding, L.i. Zhong, et al., CoMo carbide/nitride from bimetallic MOF precursors for enhanced OER performance, *Int. J. Hydrog. Energy* 46 (2021) 22268–22276.
- [44] X. Wang, X. Zhou, C. Li, et al., Asymmetric Co-N<sub>3</sub>P<sub>1</sub> trifunctional catalyst with tailored electronic structures enabling boosted activities and corrosion resistance in an uninterrupted seawater splitting system, *Adv. Mater.* 34 (2022) 2204021.